Material-Engineered Bioartificial Microorganisms Enable Efficient Waterborne Viruses Scavenging

Huixin Li
Zhejiang University
Yihao Cui
Zhejiang University
Jiake Lin
Zhejiang University
Ying Zhang
Zhejiang University
Haibin Hao
Zhejiang University
Yang Wang
Nantong University
Yan Xu
Beijing Institute of Microbiology and Epidemiology
Zi-Hao Nie
Sichuan University
Yuemin Zhou
Zhejiang University
Xiao-Yu Wang
Zhejiang University
Ruikang Tang (rtang@zju.edu.cn)
Zhejiang University https://orcid.org/0000-0001-5277-7338

Article

Keywords:

Posted Date: August 25th, 2022

DOI: https://doi.org/10.21203/rs.3.rs-1948180/v1

Version of Record: A version of this preprint was published at Nature Communications on August 3rd, 2023. See the published version at https://doi.org/10.1038/s41467-023-40397-5.

Abstract

Material-based tactics have attracted extensive attention for promoting the functional evolution of organisms. Aiming at design of steerable bioartificial organisms to scavenge pathogenic waterborne viruses, we engineer Paramecia (Para), single-celled water clarifying microorganisms, through integrating a semiartificial and specific virus-scavenging organelle (VSO). To achieve the virus-scavenging function, Fe_3O_4 magnetic nanoparticles modified with a virus-targeted antibody (MNPs@Ab) were efficiently integrated into vacuole organelles of natural Para during the feeding process. The carboxyl group-modified VSO persists inside Para for a long period without compromising the swimming ability. Compared with natural Para, which has no capture specificity and inefficient biodegradation, the VSO-engineered Para (E-Para) efficiently gathers all the viruses in water, and confines them inside the VSO. Moreover, the captured viruses are completely deactivated inside VSOs, because their acidic environment symbiotically elevates the peroxidase-like activity of nano Fe_3O_4, resulting in the production of virus-deactivated hydroxyl radicals (•OH). After treatment, E-Para can be readily recycled using magnetic fields, thus avoiding further environmental contamination. This strategy has the potential to promote functional evolution of organisms by materials-based artificial organelles, which tailors natural Para into a "living virus scavenger", leading to clearance of waterborne viruses with high efficiency and no extra energy consumption.

Introduction

The integration of functional nanomaterials and organisms can promote the functional evolution of living organisms with addressable biological responsiveness and broad application prospects[1–3], thus attracting extensive attention in the fields of biomedicine[4–6], microrobot fabrication[7–9], energy conversion[10,11] and environmental science[12]. Intriguingly, magnetotactic bacteria (MTB) are a typical example of organisms that regulate their own biological functions using magnetic materials[13,14]. MTB feature organelles known as magnetosomes, that contain magnetic nanoparticles enveloped by lipid bilayers, which play a vital role in the maintenance of magnetotaxis and survival of MTB[15,16]. Of note, the compartment of the magnetosome acts as a potential gate for differentiation of the pH or redox between the vesicle and the cellular environment[17]. Inspired by MTB, dynamic subcellular compartments are favorable for material integration since they can shield biological clearance while maintaining relative stability in the intracellular environment, representing a key element for organism modification. However, although the material-based evolution of organisms has attracted broad interdisciplinary interest, the strategies to fabricate the abovementioned material-integrated organelles remain inadequately exploited.

Organisms, such as ciliates are the most important grazers of bacteria in aquatic environments. They play an essential role in the effective operation of biological waste-water[18,19]. Due to their great biodegradation potential, some attempts have been made to use ciliates to address water environment problems[20]. However, waterborne viruses, especially some with ultrasmall size and environmental resistance features, such as enterovirus 71 (EV71), are difficult for ciliates to remove and disinfect, not to

mention the conventional techniques such as membrane filtration and organic solvent treatment[21]. Specifically, membrane filtration such as ultrafiltration and nanofiltration can eliminate viruses from water, but the removal efficiency depends on the high requirements for influent quality[22]. In regard to common disinfection methods like chlorination, ozonation and UV radiation, the toxic disinfection by-products or the requirement of energy consumption is unfriendly to the environment (Supplementary Table 1)[23,24]. In addition to these conventional technologies, the capture and elimination of viruses from water using biological system is biofriendly, and such a process relies on biological instinct and requires no energy at all. However, to the best of our knowledge, the utility of microorganisms to remove waterborne viruses has not been reported yet. Taking advantages of the water treatment capabilities of ciliates microorganisms, engineering them with artificial virus-processing modules may endow them with the ability to deal with viruses in water.

Herein we propose to engineer native Paramecium (Para), a single-celled free-living ciliate, into a virus-scavenging biorobot by implanting semiartificial organelles, which will facilitate the capture and clearance of waterborne viruses in aquatic environments. Para can accumulate and ingest food particles through its cytostome and form vacuoles to circulate through the cell[25]. The vacuoles enable highly dynamic membrane fusion and substance exchange, which will enable the construction of artificial subcellular organelles inside Para[26,27]. Taking advantage of the feeding mechanism of Para, the particulate materials, such as inorganic nanomaterials and QDs, can be directly loaded into vacuoles of Para through a ciliated groove[25]. The ingested materials halt the digestion and egestion of intrafood vacuoles[28], thus maintaining a long-life span inside the vacuoles. The vacuole-based ingestion of material particulates is common in single-celled protozoa and could be developed as a general modification strategy.

Accordingly, we introduced a specific virus-scavenging organelle (VSO) inside Para by integrating Fe_3O_4 magnetic nanoparticles modified with a virus-targeted antibody (MNPs@Ab) into vacuoles via a feed process (Fig. 1a). The obtained VSO modules had a long life span inside the engineered Para (E-Para) and enabled virus capture by the presence of specific antibodies in VSOs during the fusion of virus-loaded vacuoles and VSOs. Inside VSOs, the acidic environment containing a large amount of hydrogen peroxide (H_2O_2) stimulated the peroxidase-like activity of MNPs[29] and generated hydroxyl radicals via the Fenton reaction[30], leading to efficient deactivation of viruses (Fig. 1b). After capturing the viruses, E-Para was efficiently collected by an external magnet to minimize environmental pollution (Fig. 1c). The E-Para scavenges pathogenic viruses from environmental water, representing a promising biorobot to control waterborne diseases and purify environmental water. Our findings provide a new concept for promoting the functional evolution of living organisms with semiartificial organelles engineered by functional nanomaterials.

Results

Engineering of Para by VSO

Fe_3O_4 magnetic nanoparticles (MNPs) were synthesized by a solvothermal method using sodium citrate as a modifier. The powder X-ray diffraction (pXRD) spectra confirmed the crystallinity of the obtained MNPs (Supplementary Fig. 1). Since the surface chemistry of MNPs may influence their stability in Para and the cytotoxicity effect on Para, we employed sodium citrate and polymers, including polyethyleneimine (PEI), polyethylene glycol (PEG), and polyacrylic acid (PAA), to modify MNPs, which were then incubated with Para for 2 hours. According to the remaining Fe content inside Para (Supplementary Fig. 2) and the cytotoxicity assay (Supplementary Fig. 3), sodium citrate-modified Fe_3O_4 (Fe_3O_4@sodium citrate) enabled efficient in vivo retention and showed less cytotoxic than the other modifiers. Thus, trisodium citrate dihydrate was added during the synthesis of the MNPs before antibody modification. The successful coating of sodium citrate on the MNP surface was confirmed by examining the characteristic peaks of the C–O stretching vibrations at 1396 cm^{-1}, C = O stretching vibrations at 1597 cm^{-1} and O–H stretching vibrations at 3416 cm^{-1} after modification using Fourier transform infrared (FTIR) spectroscopy (Supplementary Fig. 4). The carboxy group from sodium citrate serves as a reactive site for antibody modification. The EV71 monoclonal antibody was attached onto the surface of MNPs using *N*-ethyl-*N*-(3-dimethylaminopropyl) carbodiimide (EDC)/*N*-hydroxysuccinimide (NHS) conjugation chemistry. Upon antibody conjugation, the zeta potential of MNPs@Ab shifted from − 6 to -12 mV (Supplementary Fig. 5). To confirm the ability of MNPs@Ab to recognize virus, we used an enzyme-linked immunosorbent assay (ELISA), by which the MNPs@Ab preserved the binding affinity toward EV71 (Fig. 2a). Transmission electron microscopy (TEM) analysis showed dimensions of MNPs@Ab with a diameter of ∼162 nm (Fig. 2b). Moreover, the MNPs@Ab showed a saturation magnetization of ∼ 62 emu/g, which was comparable to that of the MNPs control in the presence of antibody (Fig. 2c).

The VSO was introduced by feeding Para with MNPs@Ab (200 μg/ml)-containing modified Dryl's solution (named KDS buffer, a phosphate buffer commonly used in paramecium studies)[31] for 2 hours at 25°C. Observation of natural Para using phase contrast microscopy showed transparent vacuoles (Fig. 2d), while E-Para displayed dark and isolated vacuole-like structures inside the cells (Fig. 2e). During the feeding process, the MNPs@Ab were efficiently ingested through the ciliated groove[25] and entered into Para. The intracellular MNPs@Ab were then quantitatively evaluated using inductively coupled plasma–mass spectrometry (ICP—MS), which showed 30.06 ± 2.44 μg Fe per 10^4 E-Para cells (Supplementary Fig. 6), while the Fe content in 10^4 native Para cells was 0.413 ± 0.007 μg. To verify the subcellular distribution of MNPs@Ab, ultrathin sections of E-Para were observed using TEM. The natural Para showed empty vacuoles with little *Escherichia coli (E. coli.)* as food due to starvation (Fig. 2f), whereas all the vacuoles of E-Para ingested a large amount of MNPs@Ab, indicating that new vacuoles were created after MNPs@Ab uptake (Fig. 2g).

To further prove that the VSOs were derived from food vacuoles, Para were first cultured in a feeding medium containing *E. coli* and then transferred to KDS buffer containing MNPs@Ab without *E. coli*. As shown in the ultrathin section, MNPs@Ab and *E. coli* were colocalized in the same food vacuoles, suggesting that the newly ingested MNPs@Ab fused into old *E. coli.*-containing food vacuoles that

formed before MNPs@Ab uptake (Supplementary Fig. 7). Moreover, the food vacuoles fused with each other during their circulation inside Para, suggesting that MNPs@Ab interacts with the subsequently ingested food (Supplementary Fig. 8). Furthermore, the MNPs@Ab-laden vacuoles were stable in Para for at least 24 hours, exhibiting the stability of VSO in E-Para (Supplementary Fig. 9).

The effect of VSO on the biological properties of E-Para was further examined. To assess the cytotoxicity of the implanted VSOs, we calculated the survival rate of Para after coincubation with a series concentration of MNPs@Ab[32]. The results showed that MNPs@Ab exhibited minimized cytotoxicity to Para at concentrations up to 200 μg/ml, manifesting acceptable biocompatibility (Fig. 2h). To estimate if the MNPs@Ab affect the athletic performance of Para, we evaluated the movement speed of the E-Para. Compared with that of natural Para (Supplementary Video 1), the speed of the E-Para decreased slightly, which might be attributed to the increased weight of the Para due to the VSO implantation, but there was no significant difference according to the swimming speed (Fig. 2i) and direction (Supplementary Video 2). Moreover, the magnetic hysteresis loop of E-Para showed superparamagnetic characteristics similar to those of MNPs@Ab, while natural Para was diamagnetic (Fig. 2j). These results indicated that the E-Para remained active while obtaining superparamagnetic features.

Virus capture by E-Para

To investigate whether the virus was captured by VSO, E-Para or Para was placed in EV71-contaminated aqueous solution for 4 hours at 25°C to allow viruses ingestion. The Para and ingested viruses were then observed using confocal laser scanning microscopy (CLSM). Although red dye-labeled EV71 was observed in both groups, E-Para captured more viruses than the natural Para, demonstrating that VSO enhanced the virus capture capacity (Fig. 3a, b). Moreover, we found the red signals of viruses were completely colocalized in the VSO inside the E-Para (Fig. 3a, b). Three-dimensional construction image of E-Para also convinced that the viruses were localized inside the cell but not absorbed on the cell surface. We also used cross-section of E-Para to confirm that the EV71 was captured by MNPs@Ab (Supplementary Fig. 10).

To further investigate whether the antibody on MNPs@Ab can improve capture efficiency, we placed MNPs, MNPs@Ab, Para engineered with MNPs that has no antibodies (Para-MNPs), and E-Para into EV71-contaminated water with an EV71 titer of $1{\cdot}10^3$ PFU/ml (a level comparable to the reported enterovirus titer in environmental water[33]) and determined the remaining virus in suspension after 24 hours by RT—qPCR. The MNPs@Ab only elevated the capture efficiency by 33% compared with MNPs because the instability of nanoparticles in solution[34,35] hindered the antibody-dependent capture process (Fig. 3c). In addition, the E-Para completely removed the virus from the solution, while both Para and Para-MNPs were unable to clear the virus effectively during incubation, proving the significant improvement in virus capture by the presence of antibody (Fig. 3c). The remaining viruses in the supernatant were also validated using indirect immunofluorescence analysis (IFA). The results showed that numbers of infected rhabdomyosarcoma (RD) cells were reduced after treatment with E-Para (Fig. 3d), which was consistent with the RT—qPCR results, revealing the preferable virus capture ability of

E-Para over Para. These results reflected that VSO plays important roles in the virus capture process. The current challenge of waterborne disease control is that the small size and quite low titer in environmental water makes virus clearance extremely difficult using conventional filter devices. However, we found that E-para showed high efficacy for capturing virus with smaller size (approximately 20 nm) and with lower titer in an effective and environmentally friendly manner without the need for extra devices.

We then examined the virus capture ability of E-Para under different virus titers in the presence of a fixed number of E-Para (8000 cells/ml). As the virus titer in solution ranged from 1.6×10^3 to 1.6×10^6 PFU/ml, treatment with E-Para after 24 hours resulted in a more than 3 orders of magnitude reduction in viral titers, while the natural Para-treated solutions decreased viral titers by only one order of magnitude (Fig. 3e). All sets of data confirmed the markedly boosted virus capture efficiency of E-Para, validating that the implantation of VSOs contributed to the upgrade of the virus capture efficiency. The virus-capturing efficiency of E-para or Para over time was further explored. For Para, only 56.5% of viruses were captured, leading to less than 1 Log PFU/mL decrease of viral titer after treatment for 4 hours, and the viral titer hardly decreased after that. In contrast, the capture efficiency of E-Para continued to increase over time and eventually reached 100% after 24 hours of incubation (Fig. 3f), indicating that the VSO remained stable inside E-Para and drastically improved the virus capture efficiency.

Disinfection of virus by E-Para

The virus disinfection effect of E-Para was assessed by examining the infectivity of E-Para-captured virus using plaque-forming assays. After EV71 capture for 24 hours, the viruses inside Para and E-Para were released by cell lysis treatment and were then used to infect RD cells to determine remained infectivity. As a control, cell lysis treatment with SDS lysis buffer showed little effect on viral infectivity (Supplementary Fig. 11). Of note, when the environmental virus titer was $1\cdot10^3$ PFU/ml, the E-Para completely ingested the viruses and inactivated them (Fig. 4a, b), which indicated that the E-Para not only captured the viruses but also inactivated them. In contrast, the infectivity of viruses captured by natural Para reduced by less than 1 Log PFU/mL, suggesting that viruses were not completely inactivated by natural Para (Fig. 4a, b). Additionally, MNPs@Ab alone had no virucidal effect in water (Fig. 4a, b). Taken together, the viruses remained infectious inside vacuoles of native Para or after treatment with MNPs@Ab, while VSO inside E-Para completely disinfected the infested viruses, implying a synergic deactivation effect of MNPs@Ab in vacuoles.

Hydroxyl radical-based virus deactivation mechanism

Since ferric oxide has peroxidase-like activity in an acidic pH environment, the MNPs@Ab in VSO is capable of promoting the generation of hydroxyl radicals (•OH) by catalyzing hydrogen peroxide (H_2O_2)[30]. •OH can be used for virus disinfection due to its reactivity to almost all types of biomolecules, such as lipids and nucleotides[36–38]. To investigate the peroxidase-like activity of MNPs@Ab in vitro, electron paramagnetic resonance (EPR) spectroscopy was used. At pH 3.5, MNPs@Ab displayed stronger EPR signals (1:2:2:1) of DMPO/•OH in a dose-dependent manner (Supplementary Fig. 12) in the presence

of H_2O_2 than did the group of MNPs@Ab without adding H_2O_2, demonstrating the production of •OH in acidic pH by the presence of H_2O_2. Nevertheless, no •OH signal was detected in the MNPs@Ab and mixture of MNPs@Ab and H_2O_2 groups at pH 7.4 (Fig. 4c). Furthermore, under acidic conditions supplemented with H_2O_2, MNPs@Ab generated highly reactive •OH and decreased the infectivity of EV71 (Supplementary Fig. 13). Such results implied that the effective disinfection capacity of E-Para was based on the peroxidase-like activity of MNP@Ab under acidic conditions in the presence of H_2O_2.

As expected, the potentiated virus elimination effect of E-Para should be attributed to the elevated peroxidase-like activity of MNPs@Ab inside the VSO. 3,3,5,5-Tetramethylbenzidine (TMB), a substrate of peroxidase, can be catalyzed by ferric oxide in the presence of H_2O_2 under acidic conditions to develop a blue color with a maximum absorbance at 652 nm[29]. We therefore added TMB to KDS buffer containing E-Para to check the blue products. In accordance with expectation, both Para and E-Para cells produced a blue catalysate in vivo (Supplementary Fig. 14), while the absorbance value of TMB-treated E-para at 652 nm was evidently stronger than that of natural Para (Fig. 4d), indicating the reinforced catalytic reaction inside E-Para. Notably, the enzyme activity increased as the concentration of MNPs@Ab increased, confirming that the catalytic effect was indeed related to MNPs@Ab in VSO (Fig. 4e).

To inspect the presence of H_2O_2 inside Para, ROSGreen™, a special H_2O_2 probe that excites green fluorescence upon contact with H_2O_2 was used. Both Para and E-Para exhibited the existence of intracellular H_2O_2 (Fig. 4f), which was mainly derived from lysosomes or peroxisomes in the cytoplasm[39]. The ingestion of MNPs@Ab promoted the production of H_2O_2 over that of natural Para. However, due to the presence of MNPs@Ab, the H_2O_2 in E-Para decreased faster than that in natural Para after culture for 24 hours, suggesting that the MNPs@Ab in VSO accelerated H_2O_2 consumption (Fig. 4f, g).

There have been extensive studies illustrating that the food vacuole of Para undergoes a period with acidic pH[25,27,40], which, together with the H_2O_2 inside the vacuole, creates favorable conditions for the reaction between Fe (II) and H_2O_2 to yield •OH. We used 3'-(*p*-hydroxyphenyl) fluorescein (HPF) to track the formation of •OH. Interestingly, a larger number of aggregated green fluorescent vacuoles were observed in E-Para (Fig. 4i) than in natural Para (Fig. 4h), verifying the production of •OH inside VSO. Moreover, the colocalization of intracellular MNPs@Ab and the •OH fluorescence signal implied the crucial role of MNPs@Ab in the generation of •OH inside the vacuoles. Moreover, the quantitative fluorescence intensity of •OH showed that •OH production was significantly enhanced in E-Para and remained at a relatively high level compared with that in native Para (Fig. 4j). After incubation for 24 hours, the •OH in E-Para decreased compared with treatment for 0 hour but remained higher than that of native Para, suggesting that •OH was consumed during incubation. These phenomena indicated that the VSO in E-Para resulted in a continuously higher level of •OH than native Para, leading to redox damage to the ingested virus. Together, the VSO utilizes synergistic interplay between MNPs@Ab and the vacuole environment to realize sustained production of •OH, which enables efficient virus inactivation.

Recyclability of E-para

In the case of biosecurity issues caused by virus-captured E-Para in the water, it is essential to recover the used E-Para after treatment. However, Para are difficult to collect by conventional collection methods due to their outstanding motility. The VSO-implanted E-Para was easily recovered from water solution by an external magnet (Fig. 5a) and returned to free movement after the magnet was removed (Supplementary Video 3). The magnetic recovery efficiency of E-Para was related to the concentration of MNPs@Ab (Fig. 5b), which changed the magnetism strength (Supplementary Fig. 15). The magnetism variation of E-Para over time was investigated according to the magnetic hysteresis loop of E-Para, who exhibited identical superparamagnetic properties within 24 hours and a slight decrease in the saturation magnetization from 4.4 to 2.0 emu/g (Fig. 5c). Although the saturation magnetization of E-Para decreased over time, its impact on the magnetic recovery rate of E-Para was negligible (Fig. 5d). In addition, the magnetic recovery of E-Para in various volumes of solution was unaffected by the increasing volumes of water, indicating the availability of E-para removal without the need for extra operation of the solution (Fig. 5e). From these results, utilizing the magnetism of VSO to recover Para from water is feasible to ensure the biosafety of this tactic. The magnetic VSO enabled the ready and efficient recovery of E-Para by magnetic fields, which facilitated the subsequent detection and analysis of the viruses and avoided the risk of infection, thus ensuring the environmental friendliness and biosafety of this strategy.

Conclusions

In summary, we designed a virus-scavenging semiartificial organelle to arm Para with the ability to capture the virus, deactivate the virus, and recover the captured virus. The customized VSOs are vacuole-derived compartments composed of virus-binding Fe_3O_4 magnetic nanoparticles, which circulate inside Para since the inorganic nanoparticles block the digestion and egestion of VSOs. The E-Para served as an efficient "microfactory" to inactivate the virus in situ through an enzyme-like catalysis pathway, by which the VSO produced large amounts of hydroxyl radicals to kill the captured viruses. Unlike conventional technologies that use high pressure filtration and detrimental chemical treatment, our strategy uses materials-engineered steerable microorganisms to collect and remove viruses, which requires minimal energy and is environmentally friendly. It is worth noting that the sustainability footprints of E-Para reached 94%, while the commonly used membrane technology nanofiltration (NF) was only 61%, which convincingly demonstrates that E-Para outperforms traditional membrane technology for virus elimination in efficiency and sustainability to a certain extent (Fig. 6). Overall, our study shows promise for functional modification of microorganisms by designing a nanotechnology-based artificial organelle, which is of considerable importance for the promotion of material-based biological evolution.

Methods

Materials

$FeCl_3 \cdot 6H_2O$ (99%) was purchased from Aladdin (Shanghai, China). Trisodium citrate dihydrate and BSA were purchased from MACKLIN (Shanghai, China). EDC, NHS, DMPO and EV71 monoclonal antibody were purchased from Merck (Darmstadt, Germany). Alexa Fluor 555 dye, Celltracker Green CMFDA and secondary antibody were purchased from Thermo Fisher (Waltham, USA). A TIANamp Virus DNA/RNA Kit (#DP315) was purchased from Tiangen Biotech (Beijing, China). A One-Step TB Green PrimeScript™ RT – PCR Kit II (#RR086A) was purchased from TaKaRa (Beijing, China). TMB was purchased from Solarbio (Beijing, China). SDS lysis was purchased from Beyotime (Shanghai, China). The ROSGreen™ H_2O_2 probe was purchased from Maokang Biotechnology (Shanghai, China). HPF was purchased from AAT Bioquest (Sunnyvale, USA).

Culture of Para

Paramecium cultures were maintained in lettuce juice medium containing *E. coli.* as food. The preparation of lettuce juice medium was as follows[42,43]: fresh lettuce leaves were washed and immersed in boiling water for a few minutes and then placed in cold water to cool. Subsequently, the leaves were treated with the juicer repeatedly and squeezed out through gauze. For use as medium, the juice was diluted 1:40 with KDS buffer (2 mM $C_6H_5Na_3O_7 \cdot 2H_2O$, 0.6 mM KH_2PO_4, 1.4 mM Na_2HPO_4, 1.5 mM $CaCl_2$) and incubated with *E. coli* for 24 hours. Para were cultured in a constant temperature incubator at 25°C.

Synthesis of Fe_3O_4 magnetic nanoparticles (MNPs)

MNPs were prepared as previously reported[44–46]. Briefly, $FeCl_3 \cdot 6H_2O$ (0.1 M) and trisodium citrate dihydrate (50 mM) were first dissolved in ethylene glycol (30 ml); afterward, NaAc (1.8 g) was added with stirring. The mixture was stirred vigorously for 30 min and then sealed in a Teflon-lined stainless-steel autoclave (50 ml capacity). The autoclave was heated at 200°C, maintained for 10 hours, and then allowed to cool to room temperature. The black products were washed with ethanol and deionized water several times.

The synthesis of Fe_3O_4@PEI, Fe_3O_4@PEG and Fe_3O_4@PAA was similar to that of MNPs, except that the stabilizer was PEI, PEG or PAA instead of sodium citrate.

Preparation of Fe_3O_4 magnetic nanoparticles modified with a virus-targeted antibody (MNPs@Ab)

The MNPs@Ab was prepared by conjugating EV71 monoclonal antibody to the MNPs. The conjugation was realized through the *N*-ethyl-*N*'-(3-dimethylaminopropyl) carbodiimide (EDC)/*N*-hydroxysuccinimide (NHS) strategy[47,48]. In detail, 1 ml of MNPs (5 mg/ml) was mixed with EDC (0.1 M) and NHS (0.7 M) for 1 hour at room temperature. The remaining reagents in the coupling reaction were removed via a magnet. Subsequently, the nanoparticles were washed with phosphate-buffered saline (PBS) and finally resuspended in 1 ml of PBS. Next, 100 µl of EV71 antibody solution (1:100) was added to the activated nanoparticle suspension and incubated at room temperature for 2 hours. Any excess unconjugated EV71 antibody was also removed via a magnet. BSA (1%) was used to block the nonspecific active sites.

Construction of E-Para

Para were collected from lettuce juice medium containing *E. coli*, washed three times with KDS to remove the *E. coli* and then resuspended in KDS. Two hundred microliters of MNPs@Ab (1 mg/ml) was added to 800 µl Para solution (10000 cells/ml) to reach a final concentration of 200 µg/ml and then coincubated with Para for 2 hours at 25 °C to construct E-Para. The E-Para were then collected via a magnet and resuspended in KDS before further processing.

Survival Rate

The survival rate of Para was evaluated as previously reported[32]. Para were collected from growth medium and transferred to KDS buffer. Then, different concentrations of MNPs@Ab were added to reach final concentrations of 100, 200, 400, 800 and 1600 µg/ml. The Para were incubated for 24 hours at 25°C. Viable and nonviable cells were counted manually using a stereomicroscope (SZMN, SUNNY OPTICAL, China). Those Para that were immobile and did not preserve their typical shape were considered dead. Control experiments were performed using KDS buffer without any addition of MNPs@Ab. The survival rate (N, %) was calculated as follows:

$$N\,(\%) = \frac{N_2}{N_1} \times 100\%$$

1

where N_2 is the number of live Para after incubation for 24 hours and N_1 is the total number of Para at the start of the experiment.

Virus Capture by E-Para

E-Para (8000 cells/ml) were incubated with virus solution for 24 hours at 25 °C. Then, the E-Para-containing virus was removed by magnetic separation. The titers of virus solutions before and after treatment with E-Para were analyzed by RT–qPCR assay.

RNA isolation and RT–qPCR

Total viral RNA was extracted using a TIANamp Virus DNA/RNA Kit according to the manufacturer's instructions and then quantified by one − step quantitative real − time RT − qPCR using a One Step TB Green PrimeScript™ RT − PCR Kit II according to the manufacturer's protocol with specific primers.

Quantitative RT–qPCR was performed using an Applied Biosystems 7500 Fast Real-Time PCR System (ThermoFisher, USA). The RT–qPCR was applied to 20 µl systems (10 µl of 2X One Step TB Green RT–qPCR Buffer 4, 0.8 µl of PrimeScript 1 Step Enzyme Mix 2, 0.8 µl each of forward and reverse primers (10 µM), 0.4 µl of ROX Reference Dye II (50X)[*3], 2 µl of total RNA, 5.2 µl of RNase Free dH_2O). RT–qPCR response procedures (Stage 1: 1 cycle at 42°C for 5 min; Stage 2: 95°C for 10 s; Stage 3: 40 cycles at 95°C

for 3 s, 60°C for 30 s; Stage 4: 1 cycle at 95°C for 15 s, 60°C for 1 min, 95°C for 15 s) were applied according to the manufacturer's instructions.

The primers used for RT–qPCR are listed in Table 1[49].

Table 1
Primers used for the RT–qPCR analysis of EV71.

Primer	Sequence
EV71-F	GGCCATTTATGTGGGTAACTTTAGA
EV71-R	CGGGCAATCGTGTCACAAC

Fluorescence imaging

Fluorescence staining of EV71. One hundred microliters of virus solution was added to 500 μl of preprepared $NaHCO_3$-Na_2CO_3 buffer solution (pH=9.0), followed by 6 μl of AF555 dye solution dissolved in DMSO. The obtained mixed solution was injected into a dialysis bag and placed in normal saline for 48 hours at 4 °C.

The fluorescence staining of E-Para and Para. Cell Tracker™ Green CMFDA dye solution (1 μl) was added to 1 ml concentrated E-Para solution. The obtained mixed solution was incubated for 30 min at 25 °C. The stained E-Para and Para were washed three times with KDS to remove excess dye.

The stained E-Para or Para were coincubated with stained virus for 4 hours at 25 °C and fixed with paraformaldehyde (4%) for 12 hours at 4 °C. The fluorescence images were collected by CLSM (BX61, Olympus, Japan).

Plaque-forming assay

The infectivity of EV71 in solution and in Para was assessed by plaque-forming assays in RD cells. For EV71 in solution, the virus solutions were diluted in PBS in a dilution series of 1:10. RD cells were seeded in a 12-well plate for 48 hours, and then cells were infected with 1 ml of 10-fold viral dilutions for 1 hour at 37 °C. For EV71 in E-Para and Para, the Para-containing virus was lysed at a concentration of 1:10 in SDS lysis buffer and KDS for 10 min to release the virus in Para, and the resulting virus solution was then diluted 10-fold to infect the RD cells for 1 hour at 37 °C. The viral supernatants were replaced with DMEM containing low-melting-point agarose (1%) and FBS (2%). The cells were then incubated at room temperature for 20 min to solidify and then incubated at 37 °C for another 4-5 days. Cells were then fixed with formaldehyde (4%) for 30 min at room temperature, followed by staining with crystal violet solution (1%) for 15 min. Finally, all visible plaques were photographed and counted, and the final titers were calculated accordingly.

In vitro •OH detection by EPR

•OH generated by the Fenton-like reaction between MNPs@Ab and H_2O_2 was detected using an EPR spectrometer (A300, Bruker, USA) at room temperature. 5,5-Dimethyl-1-pyrroline-*N*-oxide (DMPO) was used as a spin trap for the detection of •OH. Then, 100 µl of DMPO (0.15 M) was added to 50 µl of MNPs@Ab solution and detected immediately after the addition of 50 µl of H_2O_2 (10 M). H_2O_2 and MNPs@Ab only were used as controls. The settings of the EPR measurement parameters were as follows: 20.5 mW microwave power, 120 G scan range and 2 G amplitude modulation.

Peroxidase-like activity of E-Para

Qualitative analysis. One hundred microliters of TMB single-component substrate solution was added to 900 µl of KDS containing Para (8000 cells/ml). The mixture of TMB and E-Para was incubated for 20 min at 25 °C in the dark. The photographs were collected with an inverted fluorescence microscope (IX73, Olympus, Japan).

Quantitative analysis. One hundred microliters of TMB single-component substrate solution was added to 900 µl of KDS containing Para (8000 cells/ml) or 900 µl of MNPs@Ab solution (200 µg/ml). The mixture of TMB and E-Para was incubated for 20 min at 25 °C in the dark, and then 100 µl of SDS lysis buffer was added and incubated for another 10 min. Then, 100 µl of the above mixed solution was added to a 96-well plate, and the absorbance at 652 nm was measured with a microplate reader (Synergy H1, BioTek, USA). Three parallel groups were set up for each sample.

In vivo H_2O_2 measurement

Qualitative analysis. The intracellular H_2O_2 levels of E-Para and Para were measured by ROSGreen™. Briefly, 500 µl of ROSGreen™ H_2O_2 Probe (10 µM) was added to 500 µl of KDS containing Para (8000 cells/ml) and incubated for 30 min at room temperature in the dark. After that, the Para were fixed with paraformaldehyde (4%) for 1 hour at room temperature, washed three times with KDS and observed by the FITC channel of an inverted fluorescence microscope (IX73, Olympus, Japan).

Quantitative analysis. Fifty microliters of ROSGreen™ H_2O_2 Probe (10 µM) was added to 50 µl of KDS containing Para (8000 cells/ml) and incubated in a black 96-well plate with a clear bottom for 30 min at room temperature in the dark. Four parallel groups were set up for each sample. The fluorescence intensity was measured and recorded by means of a fluorescence microplate reader (Synergy H1, BioTek, USA) at 490 nm excitation and 525 nm emission. KDS was used as a control. The intracellular H_2O_2 level was calculated according to the fluorescence value and standard curve of H_2O_2 (Supplementary Fig. 16).

In vivo •OH measurement

Qualitative analysis. The intracellular •OH levels of E-Para and Para were measured by HPF. Briefly, 500 µl of an HPF working solution (20 µM) was added to 500 µl of KDS containing Para (8000 cells/ml) and incubated for 45 min at room temperature in the dark. After that, the E-Para and Para were fixed with paraformaldehyde (4%) for 1 hour at room temperature and washed three times with KDS. Then, the E-

Para and Para were observed by the FITC channel of an inverted fluorescence microscope (IX73, Olympus, Japan).

Quantitative analysis. The fluorescence intensity of HPF was measured by ImageJ software (Version 1.51j8, USA).

Magnetic recovery

The E-Para containing virus was collected with a magnet. The number of E-Para collected by magnetic force and the total number of E-Para were recorded manually with a stereomicroscope (SZMN, SUNNY OPTICAL, China). The magnetic recovery efficiency (M, %) of E-Para was calculated according to the following formula:

$$M\,(\%) = \frac{M_2}{M_1} \times 100\%$$

2

where M_2 is the number of E-Para collected by magnetic force and M_1 is the total number of Para.

Date availability

The authors declare that data supporting the findings of this study are available within the article and its Supplementary Information files. All relevant data are available from the corresponding author upon reasonable request.

Declarations

Acknowledgements

We are grateful to Shuangshuang Liu from the core facility platform of Zhejiang University, School of Medicine for the technical support in CLSM analysis. We are grateful to Xiaoyan Miao at the Core Facilities of Key Laboratory of Oral Biomedical Research of Zhejiang Province, Zhejiang University School of Medicine for technical assistance in Freeze Dry System. We are grateful to Siqi Wu from the Department of Physics, Zhejiang University for the assistance with MPMS characterization. We are grateful to Jiaojiao Wang from Analysis Center of Agrobiology and Environmental Sciences, Zhejiang University. We thank Xiaomin Zhang, Weilan Wang, Nianhang Rong and Xi Zheng at Bio-ultrastructure analysis Lab of Analysis center of Agrobiology and environmental sciences, Zhejiang University for technical assistance in ultrathin section preparation and electron microscopic characterization. This work was supported by the National Natural Science Foundation of China (22037005).

Author information

Authors and Affiliations

Department of Chemistry, Zhejiang University, Hangzhou, Zhejiang, China

Huixin Li, Yihao Cui, Jiake Lin, Ying Zhang, Haibin Hao, Zihao Nie, Yuemin Zhou & Ruikang Tang

Qiushi Academy for Advanced Studies, Zhejiang University, Hangzhou, Zhejiang, China

Huixin Li, Ying Zhang, Haibin Hao, Zihao Nie & Xiaoyu Wang

School of Chemistry and Chemical Engineering, Nantong University, Nantong, Jiangsu, China

Yang Wang

Laboratory of Virology, Beijing Key Laboratory of Etiology of Viral Diseases in Children, Capital Institute of Pediatrics, Beijing, China.

Yanpeng Xu

Sir Run Run Shaw Hospital, Key Laboratory of Cardiovascular Intervention and Regenerative Medicine of Zhejiang Province, School of Medicine, Zhejiang University, Hangzhou, Zhejiang, China

Xiaoyu Wang

Author contributions

X.W. and R.T conceived the project and directed the research. H.L., Y.C., J.L. and Z.N. designed and performed the experiments and analyzed the results. Y.W. helped with material synthesis. Y.X. helped with the virus production. H.L., Y.Z., H.H. and Y.Z. participated in the analysis of the data. H.L. and X.W. wrote the manuscript.

Competing interests

The authors declare no competing interests.

References

1. Guo, Z., Richardson Joseph, J., Kong, B. & Liang, K. Nanobiohybrids: Materials approaches for bioaugmentation. Sci. Adv. **6**, eaaz0330 (2020).
2. Zhu, W. et al. SupraCells: Living mammalian cells protected within functional modular nanoparticle-based exoskeletons. Adv. Mater. **31**, 1900545 (2019).
3. Li, B., Cui, Y., Wang, X. & Tang, R. Novel nanomaterial–organism hybrids with biomedical potential. Wiley Interdiscip. Rev.-Nanomed. Nanobiotechnol. **13**, e1706 (2021).
4. Zhao, Y. et al. Surface-anchored framework for generating RhD-epitope stealth red blood cells. Sci. Adv. **6**, eaaw9679 (2020).

5. Zhao, R. et al. Nanomaterial-based organelles protect normal cells against chemotherapy-induced cytotoxicity. Adv. Mater. **30**, 1801304 (2018).
6. Li, C.-X. et al. Artificially reprogrammed macrophages as tumor-tropic immunosuppression-resistant biologics to realize therapeutics production and immune activation. Adv. Mater. **31**, 1807211 (2019).
7. Soto, F. et al. Smart materials for microrobots. Chem. Rev. **122**, 5365–5403 (2022).
8. Wu, Z., Chen, Y., Mukasa, D., Pak, O.S. & Gao, W. Medical micro/nanorobots in complex media. Chem. Soc. Rev. **49**, 8088–8112 (2020).
9. Dreyfus, R. et al. Microscopic artificial swimmers. Nature **437**, 862–865 (2005).
10. Zhang, H. et al. Bacteria photosensitized by intracellular gold nanoclusters for solar fuel production. Nat. Nanotechnol. **13**, 900–905 (2018).
11. Giraldo, J.P. et al. Plant nanobionics approach to augment photosynthesis and biochemical sensing. Nat. Mater. **13**, 400–408 (2014).
12. Liu, Z. et al. Nanoporous gold-based microbial biosensor for direct determination of sulfide. Biosens. Bioelectron. **98**, 29–35 (2017).
13. Blakemore, R. Magnetotactic bacteria. Science **190**, 377–379 (1975).
14. Faivre, D. & Schüler, D. Magnetotactic bacteria and magnetosomes. Chem. Rev. **108**, 4875–4898 (2008).
15. Uebe, R. & Schüler, D. Magnetosome biogenesis in magnetotactic bacteria. Nat. Rev. Microbiol. **14**, 621–637 (2016).
16. Schüler, D. Genetics and cell biology of magnetosome formation in magnetotactic bacteria. Fems Microbiol. Rev. **32**, 654–672 (2008).
17. Schuler, D. & Frankel, R.B. Bacterial magnetosomes: microbiology, biomineralization and biotechnological applications. Appl. Microbiol. Biotechnol. **52**, 464–473 (1999).
18. Zhang, L. et al. Simultaneous removal of colonial microcystis and microcystins by protozoa grazing coupled with ultrasound treatment. J. Hazard. Mater. **420**, 126616 (2021).
19. Xu, W. et al. Rising temperature more strongly promotes low-abundance paramecium to remove microcystis and degrade microcystins. Environ. Pollut. **291**, 118143 (2021).
20. Pillai, S.C. & Subrahmanyan, V. Role of protozoa in the activated sludge process. Nature **150**, 525–525 (1942).
21. Solomon, T. et al. Virology, epidemiology, pathogenesis, and control of enterovirus 71. Lancet Infect. Dis. **10**, 778–790 (2010).
22. Chen, C., Guo, L., Yang, Y., Oguma, K. & Hou, L.-a. Comparative effectiveness of membrane technologies and disinfection methods for virus elimination in water: A review. Sci. Total Environ. **801**, 149678 (2021).
23. Krasner, S.W. et al. Occurrence of a new generation of disinfection byproducts. Environ. Sci. Technol. **40**, 7175–7185 (2006).

24. Gerba Charles, P., Gramos Dawn, M. & Nwachuku, N. Comparative inactivation of enteroviruses and adenovirus 2 by UV light. Appl. Environ. Microbiol. **68**, 5167–5169 (2002).
25. Mast, S.O. The food-vacuole in paramecium. Biol. Bull. **92**, 31–72 (1947).
26. Allen, R.D. Food vacuole membrane growth with microtubule-associated membrane transport in Paramecium. J. Cell Biol. **63**, 904–922 (1974).
27. Fok, A.K., Lee, Y. & Allen, R.D. The correlation of digestive vacuole pH and size with the digestive cycle in paramecium caudatum. J Protozool. **29**, 409–414 (1982).
28. Werlin, R. et al. Biomagnification of cadmium selenide quantum dots in a simple experimental microbial food chain. Nat. Nanotechnol. **6**, 65–71 (2011).
29. Gao, L. et al. Intrinsic peroxidase-like activity of ferromagnetic nanoparticles. Nat. Nanotechnol. **2**, 577–583 (2007).
30. Chen, Z. et al. Dual enzyme-like activities of iron oxide nanoparticles and their implication for diminishing cytotoxicity. ACS Nano **6**, 4001–4012 (2012).
31. Dryl, S. Antigenic transformation in paramecium-aurelia after homologous antiserum treatment during autogamy and conjugation. J Protozool. **6**, 25–25 (1959).
32. Kryuchkova, M. & Fakhrullin, R. Kaolin alleviates graphene oxide toxicity. Environ. Sci. Technol. Lett. **5**, 295–300 (2018).
33. Haramoto, E. et al. A review on recent progress in the detection methods and prevalence of human enteric viruses in water. Water Res. **135**, 168–186 (2018).
34. Hu, Y., Mignani, S., Majoral, J.-P., Shen, M. & Shi, X. Construction of iron oxide nanoparticle-based hybrid platforms for tumor imaging and therapy. Chem. Soc. Rev. **47**, 1874–1900 (2018).
35. Mahmoudi, M., Sant, S., Wang, B., Laurent, S. & Sen, T. Superparamagnetic iron oxide nanoparticles (SPIONs): Development, surface modification and applications in chemotherapy. Adv. Drug Deliv. Rev. **63**, 24–46 (2011).
36. Fan, J.-X. et al. Engineered bacterial bioreactor for tumor therapy via Fenton-like reaction with localized H_2O_2 generation. Adv. Mater. **31**, 1808278 (2019).
37. Kim, K., Narayanan, J., Sen, A. & Chellam, S. Virus removal and inactivation mechanisms during iron electrocoagulation: capsid and genome damages and electro-Fenton reactions. Environ. Sci. Technol. **55**, 13198–13208 (2021).
38. Giannakis, S. A review of the concepts, recent advances and niche applications of the (photo) Fenton process, beyond water/wastewater treatment: Surface functionalization, biomass treatment, combatting cancer and other medical uses. Appl. Catal. B-Environ. **248**, 309–319 (2019).
39. Circu, M.L. & Aw, T.Y. Reactive oxygen species, cellular redox systems, and apoptosis. Free Radic. Biol. Med. **48**, 749–762 (2010).
40. Muller, M. & TÖRÖ, I. Studies on feeding and digestion in protozoa. III. Acid phosphatase activity in food vacuoles of paramecium multimicronucleatum. J Protozool. **9**, 98–102 (1962).

41. Palika, A. et al. An antiviral trap made of protein nanofibrils and iron oxyhydroxide nanoparticles. Nat. Nanotechnol. **16**, 918–925 (2021).
42. Hiwatashi, K. Determination and inheritance of mating type in paramecium caudatum. Genetics **58**, 373–386 (1968).
43. Tokusumi, Y. & Takagi, Y. Ectosymbiotic role of food bacteria for paramecium: Bacterial detoxification of paramecia-killing toxin contained in wheat grass powder. Zool. Sci. **17**, 341–348 (2000).
44. Guo, S., Li, D., Zhang, L., Li, J. & Wang, E. Monodisperse mesoporous superparamagnetic single-crystal magnetite nanoparticles for drug delivery. Biomaterials **30**, 1881–1889 (2009).
45. Dong, F., Guo, W., Bae, J.-H., Kim, S.-H. & Ha, C.-S. Highly porous, Water-soluble, superparamagnetic, and biocompatible magnetite nanocrystal clusters for targeted drug delivery. Chem.-Eur. J. **17**, 12802–12808 (2011).
46. Deng, H. et al. Monodisperse magnetic single-crystal ferrite microspheres. Angew. Chem.-Int. Edit. **44**, 2782–2785 (2005).
47. Xu, C., Wang, B. & Sun, S. Dumbbell-like Au-Fe_3O_4 nanoparticles for target-specific platin delivery. J. Am. Chem. Soc. **131**, 4216–4217 (2009).
48. Moura, C.C., Segundo, M.A., das Neves, J., Reis, S. & Sarmento, B. Co-association of methotrexate and SPIONs into anti-CD64 antibody-conjugated PLGA nanoparticles for theranostic application. Int. J. Nanomed. **9**, 4911–4922 (2014).
49. Xu, Y.-P. et al. Rational design of a replication-competent and inheritable magnetic viruses for targeting biomedical applications. Small **16**, 2002435 (2020).

Figures

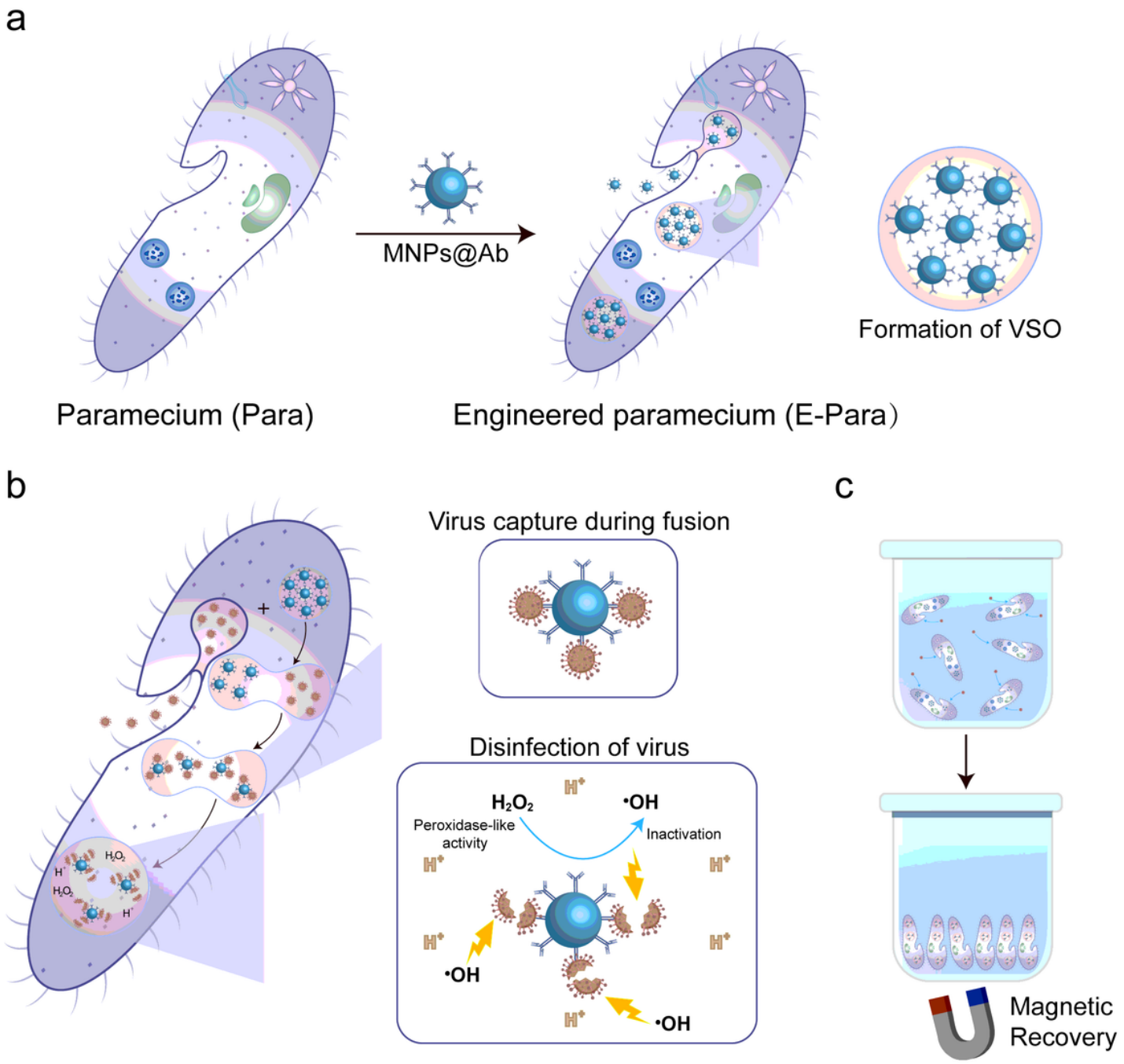

Figure 1

Schematic illustration of the preparation and working principle of E-Para. a Engineering of Para using MNPs@Ab. **b** The working principle of E-Para for virus capture and disinfection. **c** Magnetic recovery of E-Para.

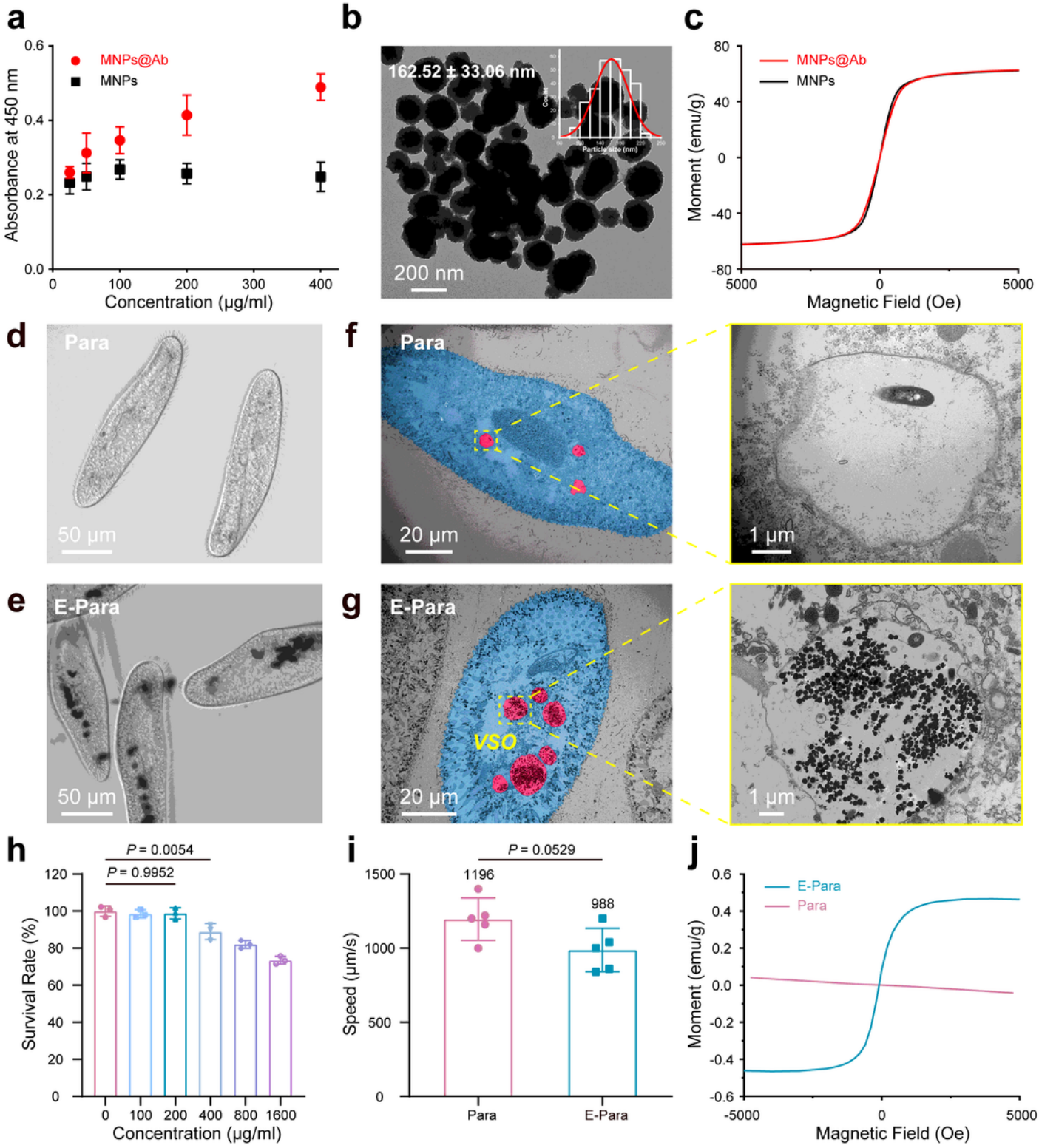

Figure 2

Construction and characterization of E-Para. a ELISA of MNPs@Ab confirmed the antibody conjugation. Data are presented as the mean ± s.d. (n = 3). **b** TEM image of MNPs@Ab and size distribution of MNPs@Ab (inset). **c** Magnetic hysteresis loop of MNPs@Ab and MNPs. **d, e** Optical microscope images of natural Para and E-Para. **f, g** TEM images of the food vacuoles in natural Para and in E-Para. The images in the yellow boxes are partially enlarged images. **h** Survival rate of Para coincubated with a

gradient series concentration of MNPs@Ab. The data are presented as the mean ± s.d. (n = 3). Statistical significance was calculated via one-way analysis of variance (ANOVA) with Tukey's multiple-comparison test. **i** Speed of natural Para and E-Para. The data are presented as the mean ± s.d. (n = 5). Statistical significance was calculated via an unpaired t test. **j** Magnetic hysteresis loop of natural Para and E-Para.

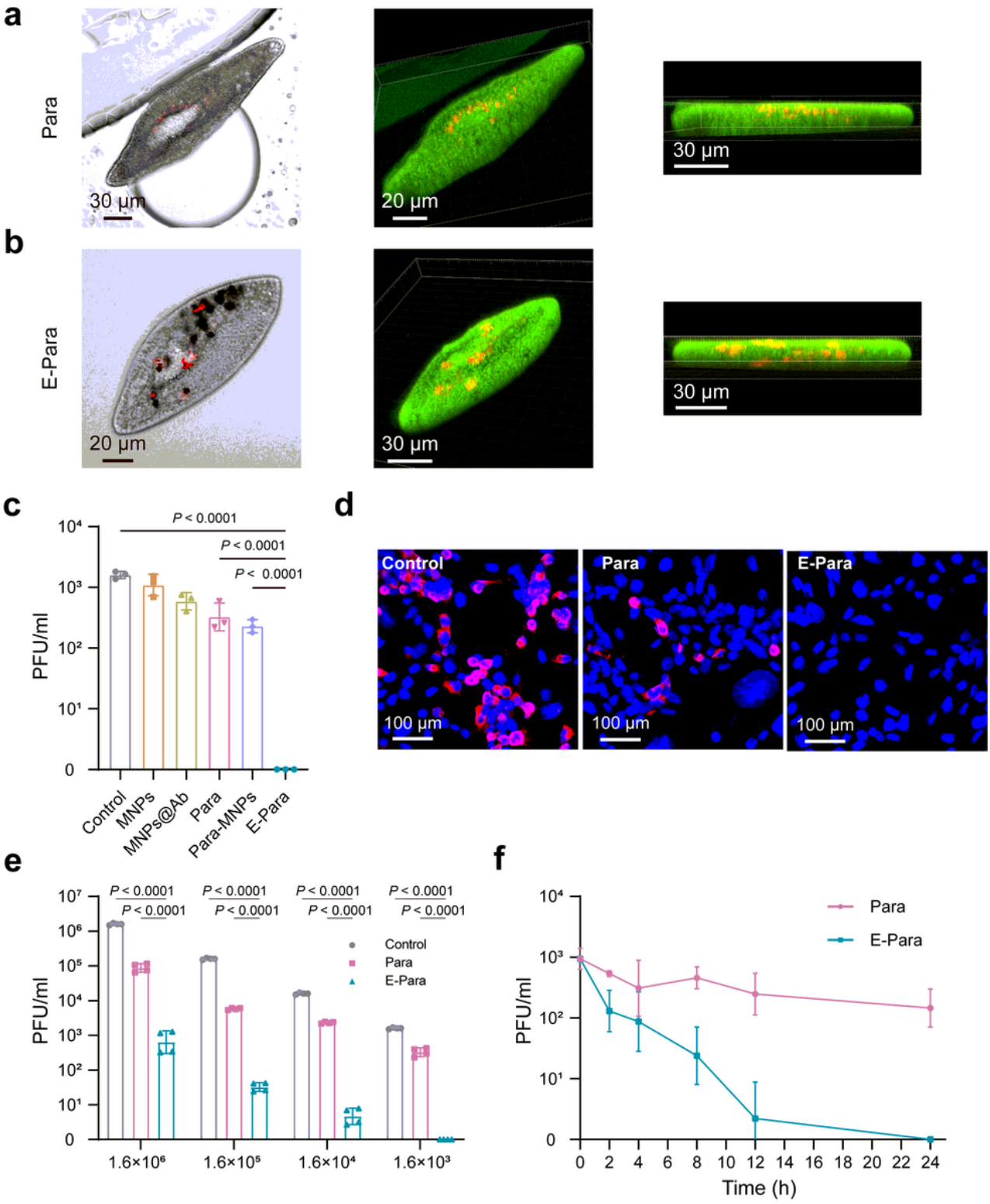

Figure 3

Virus capture by E-Para. a, b Phase and CLSM images of Para and E-Para after capturing AF555-labeled EV71 (red). In vivo EV71 was localized by merging the phase and fluorescence images. **c** Antibody-mediated specific virus capture. The data are presented as the mean ± s.d. (n = 3). Statistical significance was calculated via one-way analysis of variance (ANOVA) with Tukey's multiple-comparison test. **d** IFA results of remaining EV71 after treatment with Para or E-Para. **e** Virus capture ability of Para and E-para in the presence of different titers of EV71. The data are presented as the mean ± s.d. (n = 4). Statistical significance was calculated via two-way analysis of variance (ANOVA) with multiple-comparison test. **f** Time-dependent virus capture by Para and E-para. Data are presented as the mean ± s.d. (n = 3).

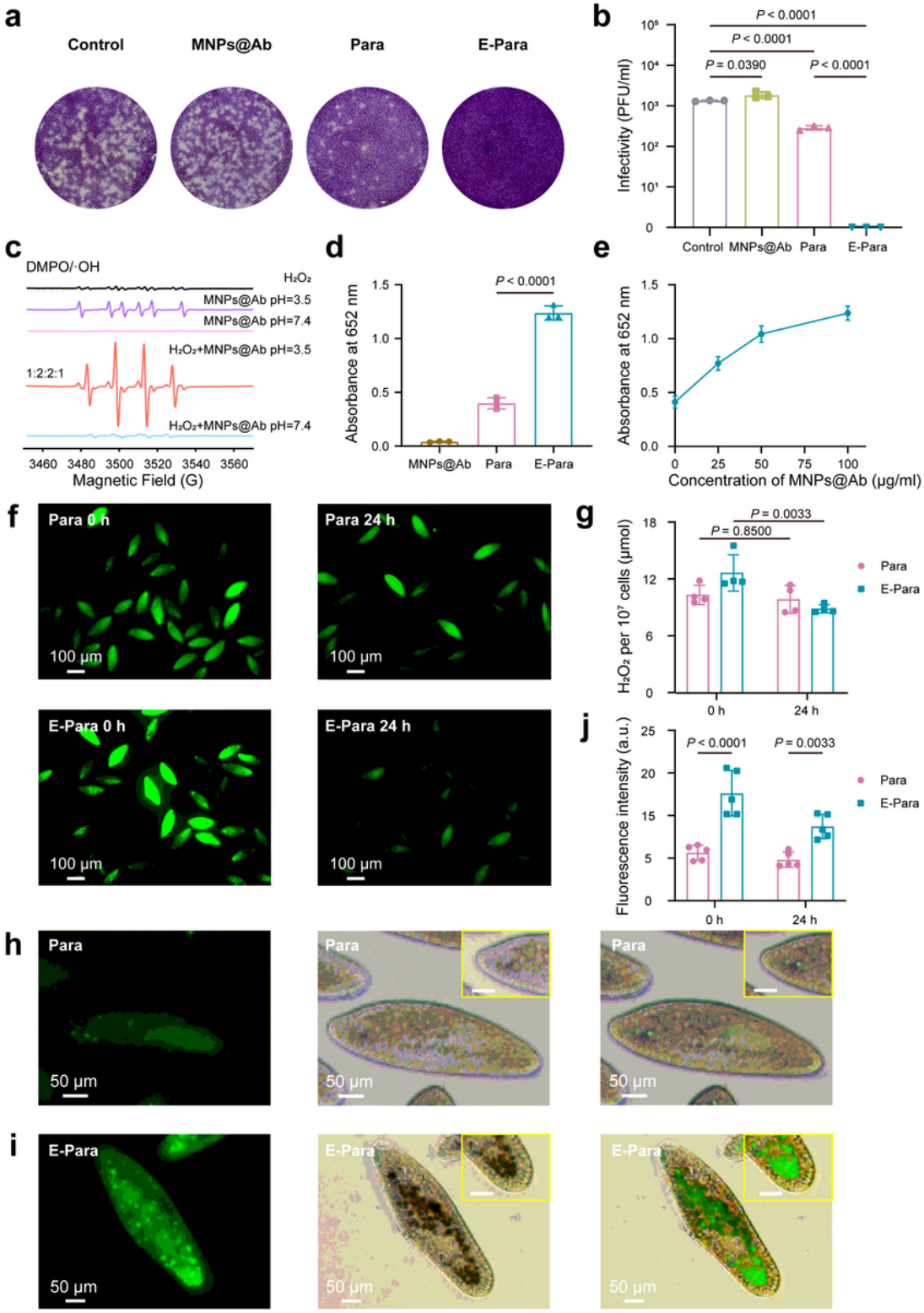

Figure 4

Disinfection effect of E-Para. a Plaque morphologies of intra-Para EV71. **b** Intra-Para EV71 titer detected by plaque-forming assay. Data are presented as the mean ± s.d. (n = 3). **c** EPR spectrum of MNPs@Ab at different pH values. **d** Comparison of the catalytic capacity of MNPs@Ab, natural Para and E-Para to TMB. Data are presented as the mean ± s.d. (n = 3). **e** The dose-dependent catalytic capacity of E-Para. The data are presented as the mean ± s.d. (n = 3). **f** Fluorescence images of Para and E-Para stained with

ROSGreen™ (a special H_2O_2 probe). **g** H_2O_2 content in Para and E-Para. The data are presented as the mean ± s.d. (n = 4). **h, i** Fluorescence images of Para and E-Para stained with HPF (a special •OH probe). The images in the yellow boxes are partially enlarged images (Bar, 20 μm). **j** Fluorescence intensity of •OH measured by ImageJ. The data are presented as the mean ± s.d. (n = 5). Statistical comparisons were made using either one-way (**b, d**) or two-way (**g, j**) analysis of variance (ANOVA) with Tukey's multiple-comparison test.

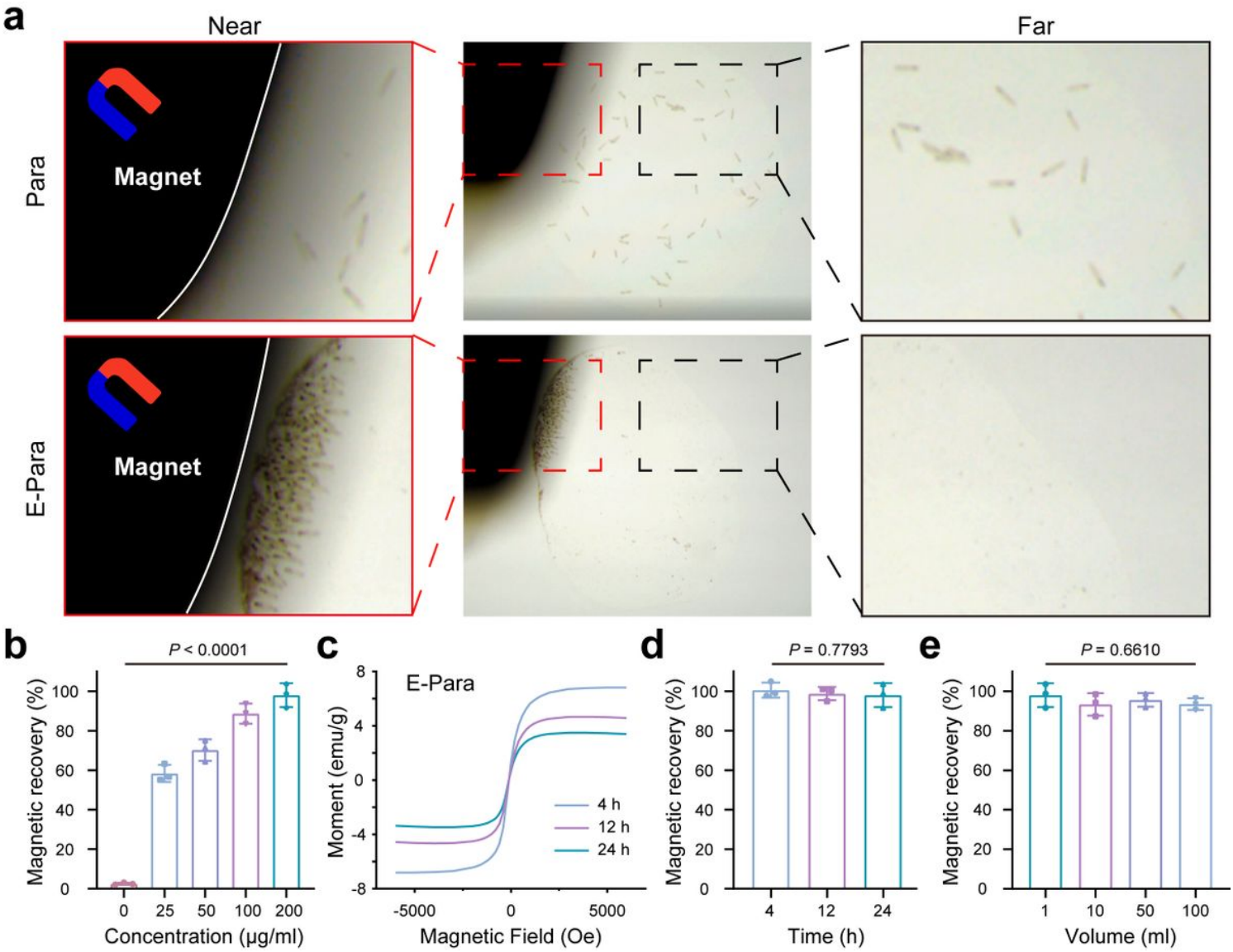

Figure 5

Magnetic directed recovery of E-Para. a Recovery of Para and E-Para with a magnet. The images were collected by a stereomicroscope. **b** Effect of incorporated MNPs@Ab concentration on magnetic recovery of E-Para. The data are presented as the mean ± s.d. (n = 3). **c** Time-dependent magnetic hysteresis loop of E-Para. **d** Magnetic recovery of E-Para at different periods. The data are presented as the mean ± s.d. (n = 3). **e** Effect of solution volume on the magnetic recovery of E-Para. The data are presented as the

mean ± s.d. (n = 3). Statistical comparisons were made using one-way analysis of variance (ANOVA) with Tukey's multiple-comparison test (**b, d, e**).

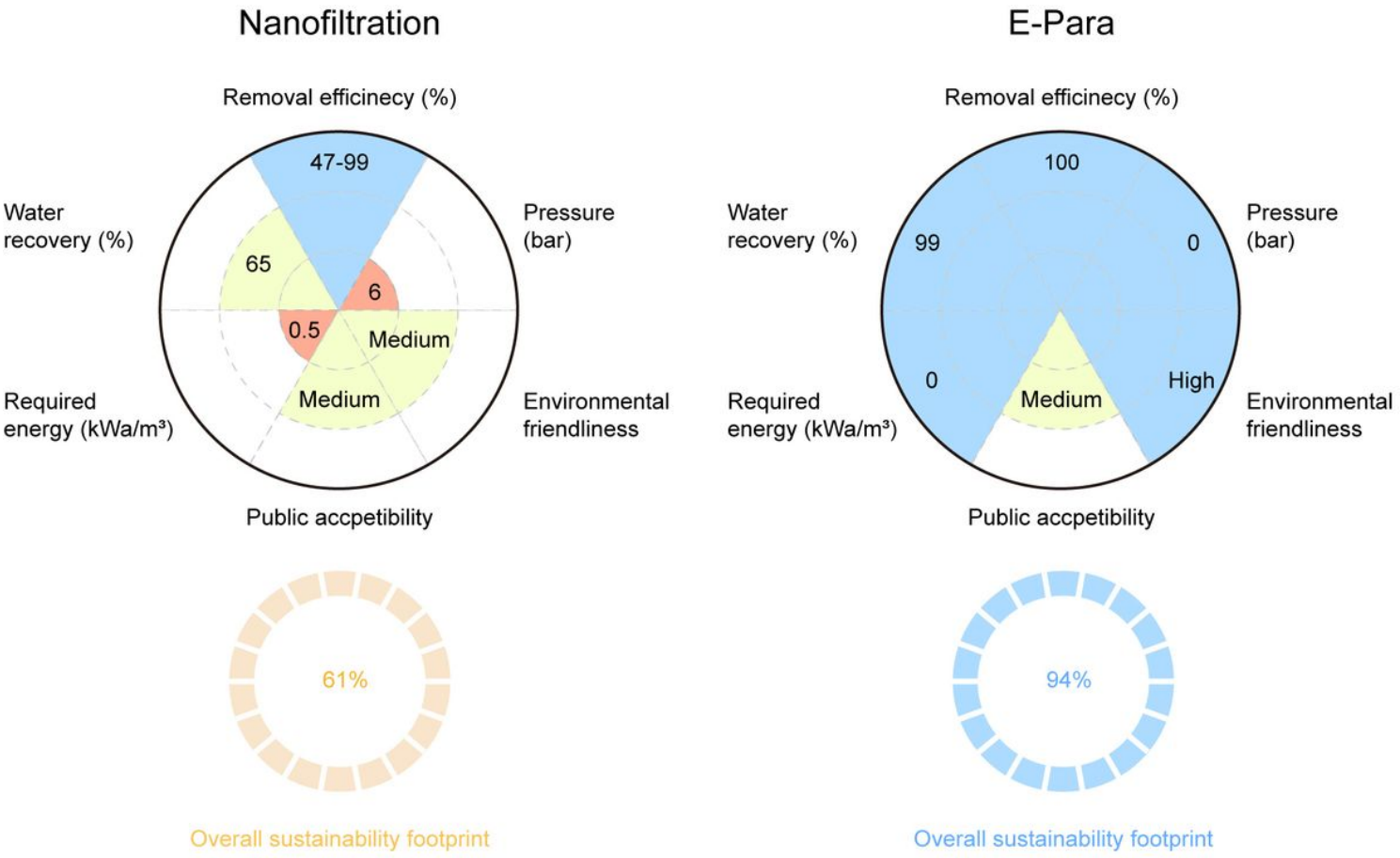

Figure 6

Sustainability footprint comparison of E-Para and NF. The factors considered are removal efficiency, pressure, environmental friendliness, public acceptability, energy consumption and water recovery. The scores of technologies in each discriminant are shown by orange (low performance), yellow (medium performance) and blue (high performance). The overall sustainability footprint is obtained by a weighted averaging of the score in each discriminant[41]. In detail, the low, medium and high performance was assigned a score (*i*) of 1, 2, 3 respectively and the overall sustainability footprint is calculated as $\Sigma^{6}_{k} = {}_{1}(i/3)_{k} \times 1/6$.

Supplementary Files

This is a list of supplementary files associated with this preprint. Click to download.

- Supplementaryinformation.docx
- SupplementaryVideo1.mp4

- SupplementaryVideo2.mp4
- SupplementaryVideo3.mp4